Spatiotemporal variability of water vapor investigated using lidar and FTIR vertical soundings above the Zugspitze

H. Vogelmann, Ralf Sussmann, T. Trickl, A. Reichert

Angaben zur Veröffentlichung / Publication details:

Vogelmann, H., Ralf Sussmann, T. Trickl, and A. Reichert. 2015. "Spatiotemporal variability of water vapor investigated using lidar and FTIR vertical soundings above the Zugspitze." Atmospheric Chemistry and Physics 15 (6): 3135–48. https://doi.org/10.5194/acp-15-3135-2015.

Atmos. Chem. Phys., 15, 3135–3148, 2015
www.atmos-chem-phys.net/15/3135/2015/
doi:10.5194/acp-15-3135-2015

Atmospheric Chemistry and Physics
Open Access

Spatiotemporal variability of water vapor investigated using lidar and FTIR vertical soundings above the Zugspitze

H. Vogelmann, R. Sussmann, T. Trickl, and A. Reichert

Karlsruhe Institute of Technology, IMK-IFU, Garmisch-Partenkirchen, Germany

Correspondence to: H. Vogelmann (hannes.vogelmann@kit.edu)

Received: 18 August 2014 – Published in Atmos. Chem. Phys. Discuss.: 14 November 2014
Revised: 6 March 2015 – Accepted: 10 March 2015 – Published: 19 March 2015

Abstract. Water vapor is the most important greenhouse gas and its spatiotemporal variability strongly exceeds that of all other greenhouse gases. However, this variability has hardly been studied quantitatively so far. We present an analysis of a 5-year period of water vapor measurements in the free troposphere above the Zugspitze (2962 m a.s.l., Germany). Our results are obtained from a combination of measurements of vertically integrated water vapor (IWV), recorded with a solar Fourier transform infrared (FTIR) spectrometer on the summit of the Zugspitze and of water vapor profiles recorded with the nearby differential absorption lidar (DIAL) at the Schneefernerhaus research station. The special geometrical arrangement of one zenith-viewing and one sun-pointing instrument and the temporal resolution of both instruments allow for an investigation of the spatiotemporal variability of IWV on a spatial scale of less than 1 km and on a timescale of less than 1 h. The standard deviation of differences between both instruments σ_{IWV} calculated for varied subsets of data serves as a measure of variability. The different subsets are based on various spatial and temporal matching criteria. Within a time interval of 20 min, the spatial variability becomes significant for horizontal distances above 2 km, but only in the warm season ($\sigma_{\mathrm{IWV}} = 0.35$ mm). However, it is not sensitive to the horizontal distance during the winter season. The variability of IWV within a time interval of 30 min peaks in July and August ($\sigma_{\mathrm{IWV}} > 0.55$ mm, mean horizontal distance = 2.5 km) and has its minimum around midwinter ($\sigma_{\mathrm{IWV}} < 0.2$ mm, mean distance > 5 km). The temporal variability of IWV is derived by selecting subsets of data from both instruments with optimal volume matching. For a short time interval of 5 min, the variability is 0.05 mm and increases to more than 0.5 mm for a time interval of 15 h. The profile variability of water vapor is determined by analyzing subsets of water vapor profiles recorded by the DIAL within time intervals from 1 to 5 h. For all altitudes, the variability increases with widened time intervals. The lowest relative variability is observed in the lower free troposphere around an altitude of 4.5 km. Above 5 km, the relative variability increases continuously up to the tropopause by about a factor of 3. Analysis of the covariance of the vertical variability reveals an enhanced variability of water vapor in the upper troposphere above 6 km. It is attributed to a more coherent flow of heterogeneous air masses, while the variability at lower altitudes is also driven by local atmospheric dynamics. By studying the short-term variability of vertical water vapor profiles recorded within a day, we come to the conclusion that the contribution of long-range transport and the advection of heterogeneous layer structures may exceed the impact of local convection by 1 order of magnitude even in the altitude range between 3 and 5 km.

1 Introduction

Water vapor plays a key role in weather and climate phenomena and is the most important greenhouse gas (e.g., Harries, 1997; Kiehl and Trenberth, 1997; Trenberth et al., 2007). However, the feedback between the anthropogenic (CO_2-driven) temperature increase and the influence of water vapor is far from understood (e.g., Wagner et al., 2006). Furthermore, climate projections still suffer from inaccurate parameterizations of water vapor absorption processes within the radiation code of general circulation models (e.g., Turner and Mlawer, 2010). Understanding the role of water vapor in the climate system is particularly complex because water vapor is the only trace compound in the atmosphere appearing

in all three states of matter. This involves a variety of factors, e.g., the possibility of latent heat transport (thereby damping latitudinal temperature gradients) and the fact that precipitation is the largest sink of atmospheric water vapor. The latter is the main reason for the strong decrease of water vapor concentration with altitude, and it is the reason why water vapor has an average lifetime in the atmosphere of just about 9 days, shorter than for any other greenhouse gas. The short lifetime is a basis of the very high spatiotemporal variability of water vapor (Trenberth, 1998).

However, the spatiotemporal variability of water vapor on the scales relevant to weather and climate is still far from being quantitatively characterized, and the underlying processes are not well understood. Variability, for instance, may be caused by local dynamics above complex mountain terrain (which changes with season), by regional meteorological effects, or by advection on larger scales. A highly interesting question is the variance of water vapor as a function of altitude on different timescales. Previous studies at our site based on ozone and aerosol lidar profiling demonstrated that the free troposphere may be affected by regional contributions, long-range transport, and stratosphere–troposphere exchange causing strongly and rapidly changing vertical structures in the concentration profile (Eisele et al., 1999; Stohl and Trickl, 1999; Trickl et al., 2003, 2010, 2011). In particular, we frequently observed very dry and sometimes very thin layers in the free troposphere, which were associated with stratospheric intrusion events. It remains open, however, how much such processes significantly contribute to the observed variability of water vapor in the middle and upper troposphere.

For understanding the long-term changes and the variability of water vapor, high-quality vertical sounding of water vapor with high temporal density is required. During the past years, a variety of optical remote sounders has been developed for this purpose in addition to the classical radiosondes (e.g., Kämpfer, 2013). Lidars, Fourier transform infrared (FTIR) spectrometers, and microwave radiometers fulfill the requirements of frequent measurements. In particular, we developed a differential absorption lidar (DIAL) for use at the Zugspitze, which allows for continuous day- and nighttime soundings of water vapor profiles up to the tropopause (Vogelmann and Trickl, 2008). For measuring integrated water vapor (IWV), the solar FTIR technique was found to be one of the most accurate and precise ground-based sounding techniques with a precision better than 0.05 mm (2.2 % of the mean) (Sussmann et al., 2009). According to a recent validation study, the lidar and FTIR water vapor sounders used for the work presented here are in excellent agreement (Vogelmann et al., 2011).

Comparing two high-precision state-of-the-art water vapor sounders, we also found that it is necessary to use very strict temporal coincidence criteria on the timescale of minutes and a spatial matching on the scale of 100 m. Otherwise, the combined precision of the instruments will be affected by the natural variability of water vapor (Sussmann et al., 2009; Vogelmann et al., 2011). This was confirmed by Bleisch et al. (2011), who reported that in case of long distances between the locations of the intercompared instruments, atmospheric variability tends to blur out the significance of validation results. The question of co-location has also become an issue in the Global Climate Observing System (GCOS) Reference Upper Air Network (GRUAN) (Immler et al., 2010; Sun et al., 2010; Seidel et al., 2011; Fassò et al., 2014), and it was addressed when evaluating water vapor sounding validation campaigns like MOHAVE (2009), LUAMI (2008), WAVES (2006), AWEX-G (2003) (Leblanc et al., 2011; Stiller et al., 2012; Wirth et al., 2009; Adam et al., 2010; Whiteman et al., 2006). Co-location also is of relevance to ground-based validation of satellite missions and has been addressed many times (e.g., Tobin et al., 2006; Soden and Lanzante, 1996).

Table 1. Specifications of the FTIR and the DIAL on the Zugspitze.

	FTIR	DIAL
Geographical	10°59′8.7″ E	10°58′46.8″ E
Coordinates	47°25′15.6″ N	47°25′0″ N
Altitude a.s.l.	2964 m	2675 m
Vertical range a.s.l.	above 2.96 km	2.95–12 km
Typ. integration time	13.3 min	17 min
Spectral range [cm^{-1}]	micro windows	ν_{on}
	839.5–840.5	12 236.560
	849.0–850.2	12 237.466
	852.0–853.1	12 243.537

The goal of this paper is to derive quantitative information relating to the spatiotemporal variability of water vapor. The solar FTIR spectrometer on the summit of the Zugspitze (2962 m a.s.l.), and the DIAL located only 680 m to the southwest and about 288 m below provide a unique geometrical arrangement of two high-precision water vapor sounders, allowing for an advanced analysis of the spatiotemporal variability of integrated water vapor (IWV) on small scales ($\Delta t < 1$ h, $\Delta x < 1$ km).

After a brief description of the instrumental setup as well as of the FTIR and DIAL IWV data with their geometrical and temporal properties, we present the quantification of the spatial and temporal variability of IWV by statistical analysis of selected subsets of IWV data from the FTIR and the DIAL (Sects. 3.1 and 3.2). The profile-type variability of the vertical water vapor distribution is analyzed quantitatively by investigating selected subsets of DIAL soundings and by calculating a profile covariance matrix (Sect. 4). Different mechanisms driving the short-term variability of water vapor are investigated in four case studies (Sect. 5). Finally, major results are summarized (Sect. 6).

2 Instrumentation and geographical arrangement

2.1 Zugspitze solar FTIR system

Solar absorption FTIR spectrometry uses the direct radiation from the sun in the mid-infrared range as a light source. The FTIR provides total columns of numerous atmospheric trace gases. Additionally, information on the vertical distribution of trace gases can be derived (typically 2–3 degrees of freedom in a retrieval optimized for IWV) from the shape of the pressure-broadened infrared lines. Due to its principle, the solar FTIR points towards the actual position of the sun and measures slant columns/profiles that are angle corrected for consistency with vertical profiles. The FTIR instrument (Table 1) located on the summit of the Zugspitze is based on a Bruker IFS125HR interferometer and is described in detail by Sussmann and Schäfer (1997). The retrieval of IWV is based on the SFIT 2 algorithm (Pougatchev et al., 1995), which is the standard code of the Network for the Detection of Atmospheric Composition Change (NDACC). An FTIR retrieval optimized for IWV was developed recently by Sussmann et al. (2009). The precision of the IWV retrieval was estimated to be better than 0.05 mm (2.2 % of the mean).

2.2 Differential absorption lidar (DIAL)

DIAL is a laser-based remote sensing technique that provides number-density profiles of trace gases. Measurements are based on specific molecular absorption and well-established spectroscopy. The Zugspitze DIAL is operated with single absorption lines in the 817 nm band of H_2O (Table 1) for ground-based water vapor profiling in the free troposphere. In order to keep a balanced signal-to-noise ratio, a vertical resolution (VDI Guideline 4210) of 50 to 300 m is adapted dynamically to the vertical range from 2.95 to roughly 12 km a.s.l., respectively. Thus, statistical measurement uncertainties are kept below about 5 % related to a mean humidity profile throughout the free troposphere. The sensitivity limit is roughly 18 ppm at 10 km a.s.l. which can occasionally be undercut in the upper troposphere. If this is the case, the upper end of the valid measurement range is reasonably reduced to lower altitudes. The DIAL instrument is located at the Schneefernerhaus research station (UFS) on the steep southern slope of the Zugspitze at an altitude of 2675 m a.s.l. The range of the Zugspitze DIAL starts 250 m above the laboratory, slightly below the altitude of the FTIR spectrometer. The DIAL system at Schneefernerhaus/Zugspitze and the retrieval of water vapor profiles are described in more detail by Vogelmann and Trickl (2008). Water vapor profiles from the Zugspitze DIAL allow for retrieving IWV with a precision better than 0.1 mm (Vogelmann et al., 2011).

2.3 Geographical setup and IWV data selection

The Zugspitze (47.42° N, 10.98° E, 2962 m a.s.l.) is by far the highest mountain on the northern rim of the Alps. The free troposphere above this site is representative of central Europe. The mountain is above the moist boundary layer for most of the year. Due to reduced absorption losses this site is ideal for sensitive spectroscopic measurements of water vapor throughout the free troposphere. While the FTIR instrument is located on the summit of the Zugspitze the DIAL instrument is located at the Schneefernerhaus research station (UFS) on the steep southern slope of the Zugspitze at an altitude of 2675 m a.s.l., 680 m southwest of the FTIR instrument (Fig. 1).

The sun-pointing geometry of the FTIR instrument and the fixed zenith-pointing geometry of the DIAL allow for studying the differences of IWV values measured by both instruments with defined spatial and temporal matching (Fig. 1). According to reanalysis data from the National Center for Environmental Prediction (NCEP), the center of gravity of the water vapor vertical distribution above the Zugspitze is most frequently located at a rather constant altitude between 4300 m a.s.l. in summer and 4400 m a.s.l. in winter. For simplicity, it is assumed that the FTIR IWV is horizontally located at the point where the viewing direction of the instru-

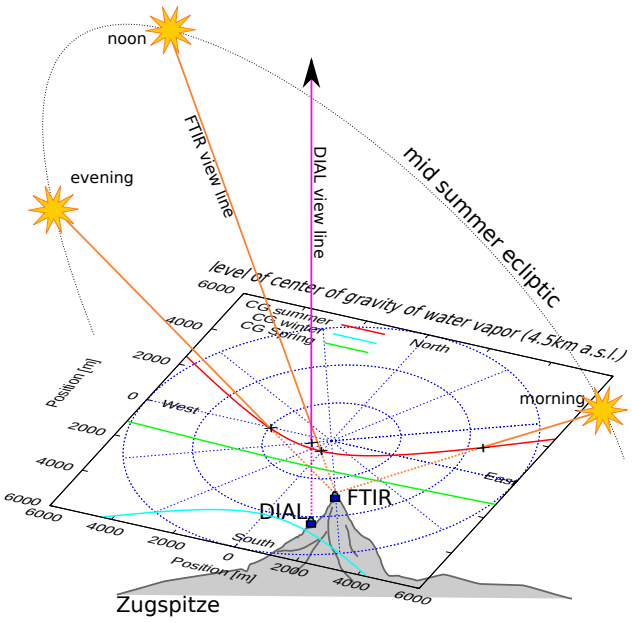

Figure 1. Geometrical setup of the IWV intercomparison between DIAL and FTIR on the Zugspitze. The DIAL is located 680 m to the southwest of the FTIR and 288 m below. The horizontal coordinate grid plane marks the mean altitude of the center of gravity of the water vapor distribution above the Zugspitze (see text) and its point of origin is vertical above the FTIR. The red, green, and blue curves in the CG plane are the trajectories of the points, where the view line (e.g., orange lines from FTIR to the sun in the case of midsummer) of the FTIR meets the CG plane in midsummer, spring, and midwinter. Consequently, the trajectories mark the horizontal position of the center of gravity of the water vapor distribution measured by the FTIR along its slanted view line. The pink line marks the fixed vertical view line of the DIAL.

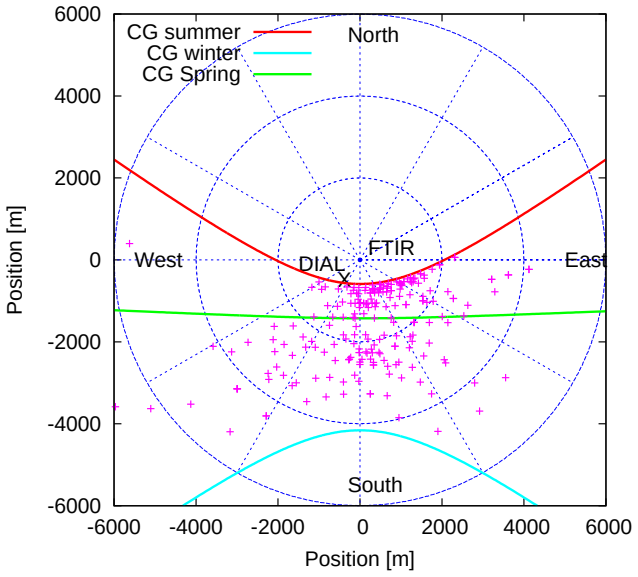

Figure 2. Trajectories of the horizontal positions of the center of gravity (CG) of the vertical water vapor distribution measured by the FTIR for IWV midsummer, spring, and midwinter. Center of gravity horizontal locations from FTIR measurements chronological coinciding with DIAL measurements ($\Delta t \leq 30$ min) are marked by crosses.

ment meets the altitude level of the center of gravity of the IWV distribution. This assumption, of course, describes the reality at high sun elevation angles better while the measured FTIR IWV is more horizontally blurred for low sun elevations close to the horizon. From this and the actual position of the sun, a rough estimate of the varying horizontal position of the IWV measured by the FTIR instrument is possible. The zenith angle of the sun defines the horizontal distance from the instrument, which may vary from less than 1 km around noon in midsummer to more than 10 km at very low sun positions. The azimuth of the FTIR IWV position is equal to the azimuth of the sun position which depends on daytime and season. In contrast to this, the horizontal position of IWV measured with the DIAL is always fixed to the location of the instrument, 680 m southwest of the FTIR site. This is illustrated in Fig. 1.

Figure 2 shows the horizontal allocation of all FTIR IWV measurements recorded concurrently ($\Delta t \leq 30$ min) with a DIAL measurement. The horizontal distance between the location of the DIAL and the horizontal position of the IWV measured by the FTIR is defined as spatial matching Δx. Figure 2 also shows the daily trajectories of the horizontal position of the center of gravity of IWV probed with the FTIR instrument for midsummer, equinox, and midwinter. In the summer season, the mean horizontal distance Δx is obviously smaller than during winter (see dashed curve in Fig. 4).

3 Variability of integrated water vapor in space and time

Of more than 350 lidar profiles recorded in the years 2007–2009, more than 250 profiles were measured during daytime (i.e., between 05:00 and 19:00 LT). In the same period, more than 3500 column measurements were made by the FTIR instrument. The systems operate with a typical integration time of 13 min (FTIR) and 17 min (DIAL). In order to obtain a quantitative measure of the water vapor variability, we analyzed certain measurement samples recorded by the two different instruments under certain spatiotemporal matching criteria for Δx and Δt. The centers of the integration time of both FTIR and DIAL were used to determine the temporal matching. We retrieved σ_{IWV} by calculating the standard deviation of the differences of IWV values from a linear model $y = a \cdot x + b$:

$$\sigma_{\mathrm{IWV}} = \sqrt{\frac{1}{n-2}\sum_{i=1}^{k}(y_i - (ax_i + b))^2}, \quad (1)$$

where y_i and x_i are the IWV values from the DIAL and the FTIR, respectively, within one sample, and n is the sample size. a and b were calculated by a regression analysis using the method of least squares. Thus,

$$\sigma_{\mathrm{IWV}} = \sqrt{\frac{1}{n-2}\sum_{i=1}^{n}\left(y_i - \bar{y} - \frac{(x_i - \bar{x})\sum_j (x_j - \bar{x})y_j}{\sum_j (x_j - \bar{x})^2}\right)^2}. \quad (2)$$

The matching criteria, amongst others, define the sample size n, which influences the uncertainty of σ_{IWV} itself. The uncertainty of σ_{IWV} is given by $\sigma_{\mathrm{IWV}}/\sqrt{(2(n-1))}$ and is illustrated by the error bars in Figs. 3–5. The inherent integration times of the instruments (roughly 15 min) cause a statistical underestimation of short-term variabilities on the scale of minutes. For the shortest time intervals investigated here (4 min), variations are statistically underestimated by factor of about 2.

3.1 Spatial variability

We decided to analyze the spatial and temporal variabilities separately for summer and winter because of two counteracting effects:

1. The special observation geometry in this study implies that the spatial overlap Δx of both soundings depends on both daytime and season. As shown in Figs. 1, 2, and 4 (dashed curve), the best spatial matching ($\Delta x < 1$ km) is achieved around midsummer in the early afternoon only (between 12:00 and 14:00 UTC), while Δx is always larger during the winter season.

2. Due to heat-driven convective dynamics in complex mountain surroundings, spatial and temporal variabilities of IWV are expected to be higher during the summer season. The convection above alpine terrain can

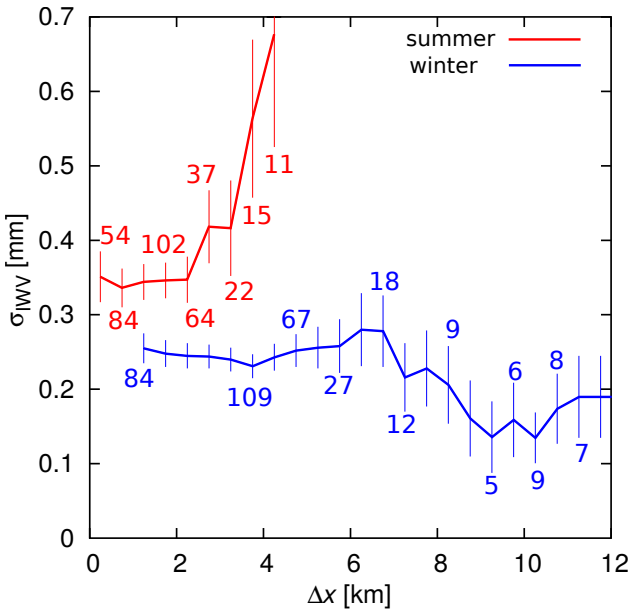

Figure 3. σ_{IWV} as a function of the horizontal distance Δx between the center of gravity of FTIR IWV and DIAL IWV in the summer season (red) and in the winter season (blue). The coincidence time interval Δt is 60 min for the blue curve and 30 min for the red curve. For geometrical reasons, the shortest distance in the winter season is 1 km. The number of measurement pairs from which σ_{IWV} was calculated is indicated by the numbers near the curves (not for all nodes). The uncertainties ($\pm\sigma$) are indicated by the error bars (for calculation see text).

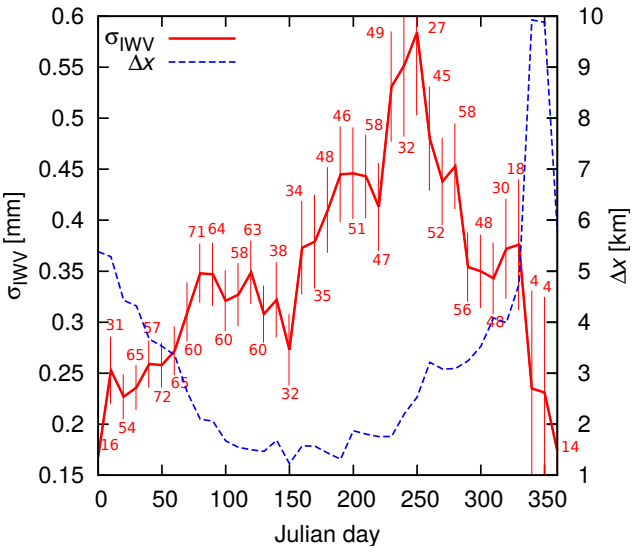

Figure 4. σ_{IWV} as a function of a Julian day. The coincidence interval is 20 min in this case; pairs within 30 days were taken into account. The quantity of measurement pairs from which σ_{IWV} was calculated is indicated by the numbers near the curve. The dashed line shows the mean horizontal distance between the pairwise soundings of IWV as a function of the season. The uncertainties ($\pm\sigma$) are indicated by the error bars (for calculation see text).

reach an altitude of about 1.5 km above the mean summit levels in summer (Carnuth and Trickl, 2000; Kreipl, 2006). During all other seasons, the convection usually does not even reach the summit of the Zugspitze and our measurement range.

For determining the spatial variability of IWV, we calculated σ_{IWV} as a function of varied spatial matching Δx by using measurement pairs within a time interval of $\Delta t = 30$ min (summer) and $\Delta t = 60$ min (winter). As mentioned above, it was shown that for a good agreement of both systems, very tight spatial and temporal matching criteria are mandatory (Vogelmann et al., 2011). Figure 3 (red curve) shows σ_{IWV} as a function of the horizontal distance of the probed volumes in the summer season. While σ_{IWV} constantly remains around 0.35 mm for $\Delta x < 2$ km, it rises to values of more than 0.65 mm at a distance of $\Delta x = 4$ km. This result shows that the variability depends on the spatiotemporal matching. Up to $\Delta x = 2$ km, the temporal variability within the selected time interval ($\Delta t = 30$ min) predominates. For larger distances, the contribution of spatial variability becomes significant.

In contrast to this, σ_{IWV} is not increasing with Δx in the winter season (Fig. 3, blue curve). This is in agreement with the assumption that local convection does not reach the vertical measurement range during the winter season and that the IWV variability is probably dominated by horizontal advection of filamentary structures in the free troposphere from very different source regions. Consequently, the observed variability during winter is due to larger spatial scale processes (compared to local convection in summer), which would explain the absence of an increase with Δx in Fig. 3. Note that because IWV is much lower in winter than in summer, the relative variabilities (i.e., if σ_{IWV} were given in percent) are larger for the blue curve in Fig. 3. This means that advection of filaments (winter) leads to larger relative changes of IWV than local convection in summer. We will discuss this finding in more detail within the context of the variability of the vertical water vapor profile in Sect. 4. Figure 3 also indicates that σ_{IWV} even shows a trend towards lower values for distances above 6 km. We explain this by the fact that measurements with large horizontal mismatch ($\Delta x > 6$ km) require extraordinarily calm and clear weather conditions, because the FTIR instrument requires a cloudless field of view and a sun position close to the horizon.

Figure 4 shows σ_{IWV} as a function of the Julian day. Here, counteracting effects can be observed. While the mean horizontal distance (dashed curve) is low in the summer season ($\Delta x < 2$ km), it reaches up to almost 10 km around midwinter. The variability over the entire field of horizontal distances within a certain time interval (e.g., 20 min) reaches its maximum of almost 0.6 mm when the temperature peaks around the end of July. We assume that this is a direct effect of the

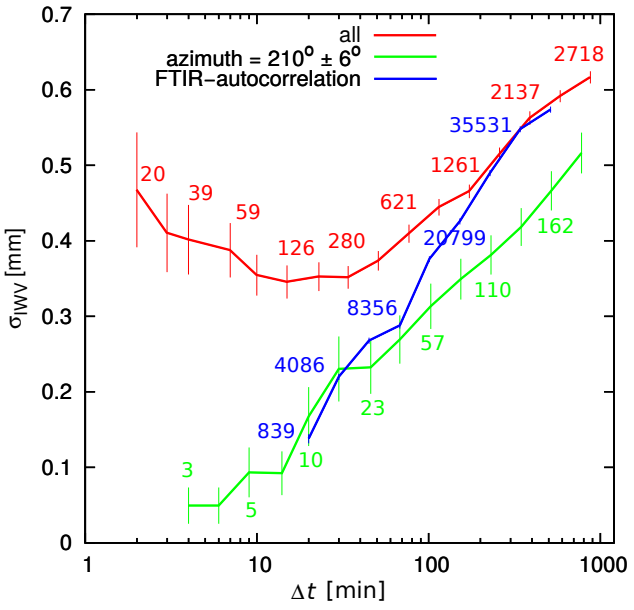

Figure 5. Variability as a function of the length of the time interval. The red curve shows σ_{IWV} from all measurements with no geometrical restrictions as a function of the length of the time interval in which data were taken into account. The green curve only includes measurements recorded in the early afternoon when the volume matching peaks with a sun azimuth of $210 \pm 6°$. The blue curve only shows σ_{IWV} of IWV values from the FTIR instrument. The quantity of measurement pairs from which σ_{IWV} was calculated is indicated by the numbers near the curves (not for all nodes). The uncertainties ($\pm\sigma$) are indicated by the error bars (for calculation see text).

heat-driven local convection, which can reach altitudes of 4.5 km at the Zugspitze site during the summer season (Reiter et al., 1983; Müller and Reiter, 1986; Carnuth and Trickl, 2000; Carnuth et al., 2002; Kreipl, 2006). The fact that the variability shows moderate values at the minimum average distance leads to the assumption that it is partially caused by local effects. As expected, the minimum variability of about 0.15 mm is observed around midwinter when temperatures are low, although the mean horizontal mismatch of both instruments is largest at this time of the year. This supports the assumption that local dynamics do not play a significant role during midwinter.

3.2 Temporal variability

For the analysis of temporal variability, we calculated the standard deviation of differences σ_{IWV} between IWV values from both instruments as a function of temporal coincidence. This was repeated for varied spatial matching criteria. When using all IWV values from both instruments without applying any geometrical matching criteria, σ_{IWV} shows a flat minimum around a coincidence interval of $\Delta t = 20$ min, see red curve in Fig. 5. About 100–300 coincident pairs contribute to the ensembles within this minimum. At first, a minimal σ_{IWV} for the shortest interval length was expected. Two different effects are responsible for the minimum around $\Delta t = 20$ min. First of all, most FTIR and lidar measurements were carried out in the morning, because there are still few clouds. As a consequence, most of the pairs with the shortest coincidence intervals are found in the morning where the spatial matching is worst (see Figs. 1 and 2). This slightly increases σ_{IWV} on the very left hand side of the red curve in Fig. 5. Secondly, many pairs with good spatial matching can be found around noon, even for somewhat larger temporal coincidence intervals. This explains the decrease of σ_{IWV} towards the minimum (red curve in Fig. 5).

When considering measurement pairs with an FTIR sun azimuth close to the position of the DIAL instrument ($210 \pm 6°$) only, σ_{IWV} is much smaller in general and has its minimum at the shortest coincidence intervals (green curve in Fig. 5). For time intervals on the minutes scale, we find $\sigma_{IWV} = 0.05$ mm, which agrees with the validated (combined) precision of our instruments Vogelmann et al. (2011).

The temporal variability of IWV can also be estimated from the standard deviation of differences of measurements recorded by the same instrument within certain time intervals. In our case, this was possible with data from the FTIR instrument only, thanks to its more frequent and continuous operation. The result is reflected by the blue curve in Fig. 5. Due to the solar FTIR's 13.3 min integration time, the curve starts at an interval length of $\Delta t = 20$ min. The blue curve begins to deviate increasingly from the green curve beyond 30 min and converges towards the red curve for larger time intervals. This corresponds to the fact that we observe a superposition of temporal and spatial variability with the solar FTIR, i.e., for larger time intervals, the FTIR instrument produces a spatial mismatch by itself: due to its sun-pointing geometry, the FTIR instrument probes a different volume after a certain time. This spatial mismatch has a significant effect for time intervals longer than 30 min.

4 Profile variability

The variability of the vertical water vapor distribution on timescales of $\Delta t \leq 5$ h was derived from water vapor number density profiles retrieved from the DIAL measurements. We built ensembles of DIAL water vapor profiles recorded within a range of time intervals (e.g., 1–5 h). After normalizing each profile using the respective ensemble mean profile, we merged all normalized profiles into a large ensemble for statistical analysis. First, we calculated the relative variance σ^2/μ^2 (with μ = ensemble mean number density) as a function of altitude for different time intervals. This is plotted on the left hand side of Fig. 6. For the shortest time interval of this investigation (1 h), the relative variance starts with a value of about 0.02. Above 5 km, the variance continuously increases to more than 0.38 at an altitude of about 11 km a.s.l.

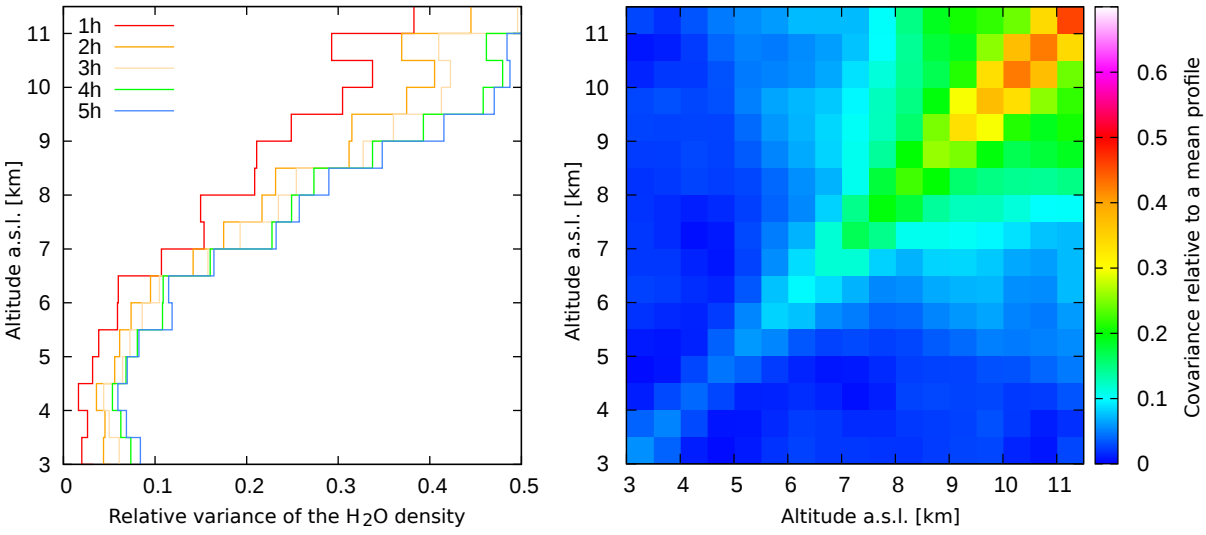

Figure 6. The short-term variability of the vertical water vapor profile is illustrated by the plot of the relative variance as a function of altitude within different time intervals (left plot). The covariance matrix (right plot) gives an idea of the interconnectivity of the variation between different altitudes.

For longer time intervals up to 5 h, the relative variance behaves quite similarly, but is shifted to higher values at all altitudes. This is in agreement with our results of IWV variability analysis, according to which longer time intervals lead to larger variabilities. In comparison to the 1 h profile, we see a more significant maximum at the lower edge at 3 km and a significant minimum at 4.5 km for longer time intervals. This enhanced increase between 3 and 4 km is, to our understanding, induced by the diurnally varying upper edge of the boundary layer during the warm season (see below).

For the lowest layer (i.e., 3–4 km), where most of the entire column above the Zugspitze site is located, we find equal relative variabilities as for IWV. This means that for a time interval $\Delta t = 1\,\mathrm{h}$, the coefficient of variation $\sigma/\mu = 0.12$. From the green curve in Fig. 5, we obtain a 1 h variability of 0.27 mm with a 60 min ensemble mean IWV of 2.33 mm, which also yields a coefficient of variation of 0.12.

In contrast to this, the relative variability increases with altitude above 5 km. This can be explained by the increasing wind speed at higher altitudes in the troposphere. The temporal variability of the water vapor density in the free troposphere at a certain altitude primarily features a horizontal variability combined with a horizontal wind velocity at this altitude. From NCEP reanalysis data, we derived an average wind speed as a function of altitude, which increases from a few meters per second near the ground to about $22\,\mathrm{m\,s^{-1}}$ in the tropopause region (Fig. 7). Similar values were reported by Birner et al. (2002) based on radiosonde data recorded above Munich (southern Germany). Depending on the pathway of the jet stream or the polar vortex, maximum wind velocities of more than $100\,\mathrm{m\,s^{-1}}$ occur occasionally (Riehl, 1962). Considering a time interval of 60 min, this means a mean horizontal spread of about 80 km around 10 km altitude with a potential increase to more than 360 km in the jet stream regime.

The general increase of the relative short-term variability of water vapor above 5 km (Fig. 6, left) seems to flatten slightly at about 10 km. This can be explained by the fact that the wind speed has its maximum here and decreases at higher altitudes. Above 9 km, the contribution of measurement errors becomes significant. The DIAL is not able to measure water vapor concentrations below 18 ppm (sensitivity limit at 10 km), which may be even lower in the tropopause region. Hence, for the calculation of variances and covariances, only profiles valid in the entire range (3–12 km) are taken into account including a statistical error calculation.

The coherence of the short-term variability of water vapor at different altitudes is analyzed using the covariance matrix of the vertical profile variability (Fig. 6, right). The covariance matrix is calculated from all normalized profiles recorded from 2007 to 2011, which are contained in the subensembles of profiles recorded within a 5 h time interval. Consequently, the diagonal of the covariance matrix is identical to the 5 h curve of the variability profile shown on the left hand side of Fig. 6. There are no significant off-diagonal values below 6 km. We interpret this as a sign of the lower altitudes not being dominated by a coherent air flow for most of the observations. This means that the horizontal flow at certain altitudes below 6 km is not or only weakly coupled to the flow above or below. The slight increase of off-diagonal values between 6 and 8 km indicates a partially coherent flow. The high off-diagonal values above 8 km indicate a large fraction of coherent flow of inhomogeneous air masses in this altitude region.

The weak coupling between different layers at lower altitudes is in agreement with the assumption of local convection

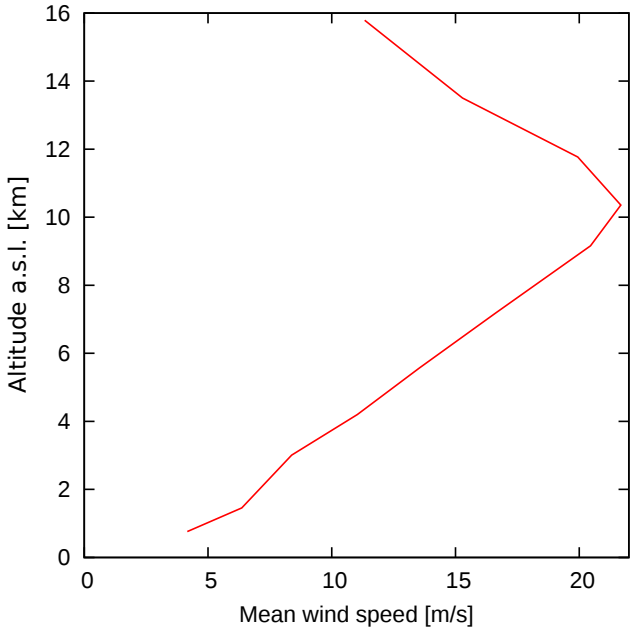

Figure 7. Mean wind speed above the Zugspitze as a function of altitude (data from the National Center for Environmental Prediction, NCEP). Under the jet stream regime, the wind velocity at 10 km can occasionally exceed 100 m s^{-1}.

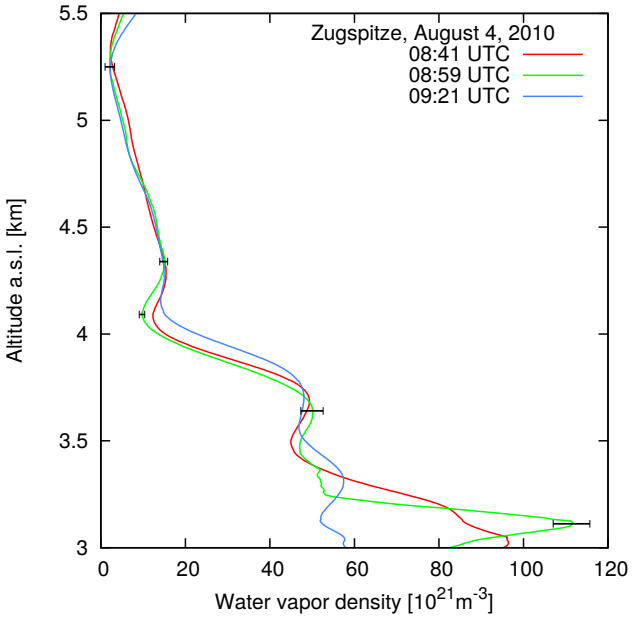

Figure 8. Short-term variability of the water vapor profile induced by local convection within a clearly confined upper edge of the boundary layer at 3.5 km under stable atmospheric conditions. The variations do not exceed a factor of 2. The example error bars ($\pm 2\sigma$) represent statistical uncertainties caused by electronic noise in the detection.

and turbulence being the dominant sources of variability in the lower part of the examined altitude range. This behavior can be described by barely interacting "bubbles" of humid air. In the upper troposphere, on the other hand, varying air masses are more coherently exchanged within the upper air flow, as a result of which layers of a wider vertical spread are affected.

5 Mechanisms driving the observed variability

In the troposphere, evaporation is the only relevant source of water vapor and precipitation the only relevant sink. Thus, water vapor is injected into the free troposphere by uplifting processes, such as local convection or large-scale warm conveyor belts. These uplifting processes cause inhomogeneity in the horizontal water vapor distribution at a certain altitude. Furthermore, air ascending to high altitudes undergoes cooling. If this air initially was humid, part of its water vapor content can be precipitated during the ascent. As a result, the absolute humidity of upper tropospheric air is low in general. Downwelling of dry air from high altitudes, in particular from the tropopause region or even the stratosphere, also produces inhomogeneity in the horizontal humidity field at the affected altitude levels. In contrast to uplifting processes, downwelling generally is not a local phenomenon. As regards the short-term variability (i.e., $\Delta t < 6$ h) of the vertical distribution of water vapor, it is reasonable to distinguish between inhomogeneity produced locally on a small scale and inhomogeneity produced remotely and transported via long-range pathways. By analyzing the measured water vapor profiles in combination with trajectory calculations from atmospheric models, we found that the short-term variability of the profiles shows contributions from both local effects and long-range transport at the same time. The short-term variability above 5 km can be attributed to the advection of a heterogeneous layer structure in most cases. Below 5 km, on the other hand, a clear assignment is not always possible. Backward trajectories were calculated from reanalysis data with the NOAA Hybrid Single-Particle Lagrangian Integrated Trajectory (HYSPLIT) vertical velocity model (http://ready.arl.noaa.gov/HYSPLIT.php, Draxler and Hess, 1998). However, the performance of a trajectory model is also limited above complex terrain and running times of several days occasionally involve large uncertainties even in the free troposphere. Sometimes several attempts are necessary to guess the correct starting altitude due to shifts in the orographic data used by the model (Trickl et al., 2010). Thus, trajectory calculations are not considered as a proof, but as support for plausibility. Our experience in the analysis of long-range transport events suggests a high reliability of free-tropospheric trajectories. In the following subsections we highlight four different types of dynamics producing short-term variability of water vapor.

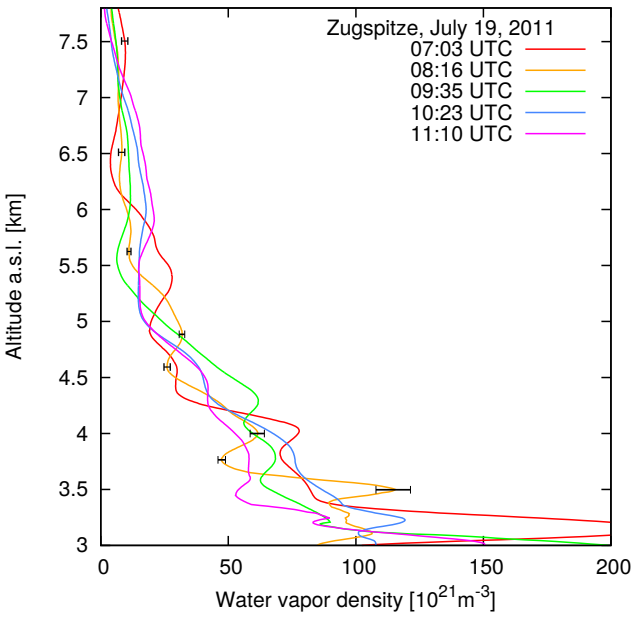

Figure 9. Short-term variability of the water vapor profile under atmospheric instability, high-reaching convection, and only a few hours before the formation of a thunderstorm. The example error bars ($\pm 2\sigma$) represent statistical uncertainties caused by electronic noise in the detection.

5.1 Local convection

5.1.1 Case studies

A case of local convection under stable atmospheric conditions (high pressure) is shown in Fig. 8. Three water vapor profiles were recorded within 40 min. The variability stops at the upper edge of the boundary layer at 3.5 km. Above this level, the water vapor distribution remains constant throughout that period. The upper edge of the boundary layer was visually verified by the upper edge of cumulus clouds located at the top of some thermals. Strongly enhanced backscatter from boundary layer aerosols was recorded up to 3.5 km. Some weaker aerosol structure that slowly moves downwards was observed above 4.5 km and even up to 7.1 km.

The situation is somewhat different under conditions of low pressure and atmospheric instability. This case is shown in Fig. 9. Five profiles were recorded within a time interval of 4 h before a heavy thunderstorm developed in the afternoon. The short-term variability of water vapor was rather high and reached far into the upper troposphere up to at least 7.5 km. Due to the travel time of upwelling air and the increasing horizontal wind speed, the variations at high altitudes (e.g., above 5 km) were less local than the variations near the ground. Cloud formation was first observed between 5.5 km and 6.5 km. However, only a few minutes later, clouds formed also above 2.5 km. Due to cloud interference, the last valid profile was recorded at 11:10 UTC (LT − 1 h). Strongly enhanced backscatter from boundary-layer aerosols was recorded up to 4.7 km already by the morning (07:03 UTC). This altitude is rather high. The latest profile at 11:10 UTC exhibits boundary-layer aerosols up to 4.2 km only and also a lower humidity compared to the profiles recorded before. In our understanding, this indicates a downflow near but outside of the thunderstorm. This downwelling air had probably lost most of its original water content during its ascent in the thunderstorm through precipitation. At 12:37 UTC (profile not shown), the extended head of the cumulonimbus cloud of the upcoming thunderstorm led to overcast at the site above 7.7 km. In addition, strong aerosol structures appear up to 7.5 km. Backward trajectory calculations (HYSPLIT) suggest that air between 6 and 7.5 km originated from the Caribbean boundary layer.

5.1.2 General discussion

During the warm season, local convection usually reaches altitudes of up to 1.5 km above summit levels (Carnuth and Trickl, 2000; Carnuth et al., 2002; Kreipl, 2006), which is about 4.5 km a.s.l. in our case. The enhanced updraft along sunny mountain slopes is also referred to as “Alpine pumping”. The slightly elevated short-term variability at lower altitudes around 3.5 km (Fig. 6, left) is attributed to local convection and the diurnal variation in the upper edge of the planetary boundary layer, which is caused by Alpine pumping. Due to the strong vertical gradient of the water vapor profile, this dominates the short-term variability of IWV in most cases when local convection significantly exceeds 3 km (which is the bottom of our measurement range). From the comparatively low mean wind speed at lower altitudes (Fig. 7), we conclude that the elevated variability here is caused by larger horizontal gradients in the water vapor concentration. This means that variations occur on smaller horizontal scales compared to higher altitudes, which underlines the fact that local processes (e.g., thermal lifts) on small scales are the dominant source. Short-term variations of the water vapor concentration at a certain altitude within the upper part of the boundary layer (i.e., 3–4.5 km a.s.l.), which are caused by local convection, are estimated to be smaller than a factor of 2. Convection penetrating into the free troposphere or even the upper troposphere can cause short-term variation factors of more than 5 at these high altitudes (e.g., Fig. 9, other observations). The presence of aerosols (enhanced backscatter) usually indicates upwelling air from the planetary boundary layer. Aerosol structures in the free troposphere are also helpful for estimating the vertical velocity of the probed air. Both cases were visually verified by the observation of cloud formation, while trajectory calculations from models are not able to resolve these small-scale local processes. However, they indicate a general downwelling for the case under stable high-pressure conditions and a general upwelling for the case under unstable low-pressure conditions.

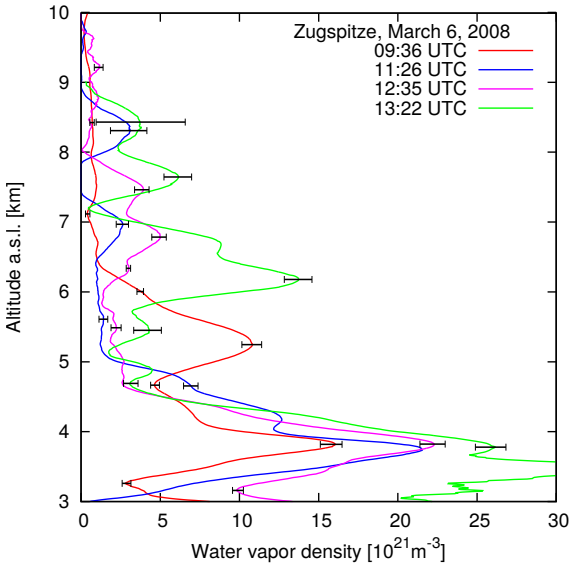

Figure 10. Example of extreme temporal variability of the vertical distribution of water vapor during a stratospheric intrusion event. Due to the advection velocity of about 11 ms^{-1} between 3 and 4 km altitude (data from radiosonde at Munich at 12:00 UTC, 100 km to the north) a time shift of 1 h corresponds to a horizontal shift of about 40 km within this altitude range. The example error bars ($\pm 2\sigma$) represent statistical uncertainties caused by electronic noise in the detection.

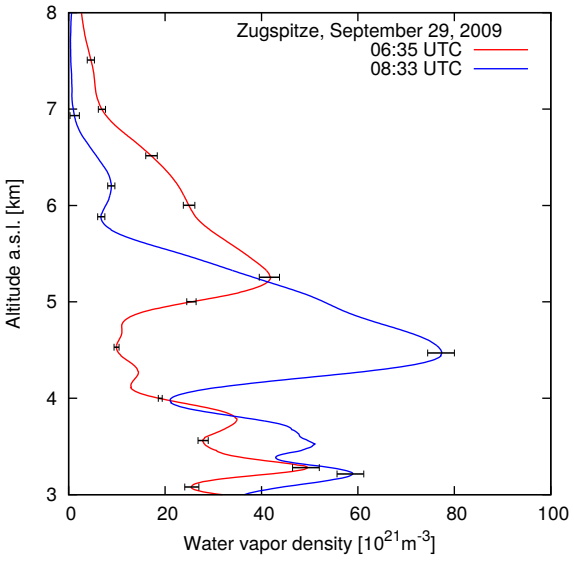

Figure 11. Example of extreme variability of the vertical distribution of water vapor under rather humid conditions. Due to a wind speed of about 16 ms^{-1} at an altitude of 4.5 km (data from radiosonde Munich at 12:00 UTC, 100 km to the north) a time shift of 2 h corresponds to a horizontal shift of about 115 km at this altitude. The two profiles were recorded within less than 2 h. The example error bars ($\pm 2\sigma$) represent statistical uncertainties caused by electronic noise in the detection.

5.2 Long-range transport

5.2.1 Case studies

Figures 10 and 11 show cases of extreme vertical variability of water vapor on a timescale of hours recorded with the DIAL. Similar scenarios have been observed many times. From these incidents we learned that the water vapor density at a certain altitude can vary by a factor of more than 30 within a few hours. Thus, the short-term variability of water vapor induced by long-range transport and the advection of very inhomogeneous layer structures can exceed the impact of local convection by 1 order of magnitude.

This is particularly pronounced for stratospheric intrusions that descend from the Arctic to central Europe. These intrusion layers occasionally become the main source of short-term variability of water vapor in the altitude range between 3 and 5 km. However, such events occur predominantly during the winter season and are accompanied by non-convective weather conditions. Under these conditions heterogeneous air masses are usually advected at a high velocity which results in a very high variability at certain altitudes even on the short timescale of 1 h. Due to the origin of these layers, stratospheric intrusion events are usually accompanied by rather dry conditions. This is illustrated by the example given in Fig. 10 where three layers of stratospheric air have been advected at the same time at different altitudes, thus creating relative variations of the water vapor density of more than a factor of 10 at certain altitudes within 4 h. The stratospheric intrusion originated above Greenland about 2–3 days before reaching our site on 6 March 2008. It exhibited several descending filaments lying upon one other. The very complex dynamics and its accompanying heterogeneous vertical layering is discussed in great detail in a separate publication including a 4-day forward trajectory calculation for this case (Trickl et al., 2014, and references therein). Stratospheric intrusions into the lower free troposphere usually occur in the winter season with a frequency of roughly 4 to 10 times per month above the Zugspitze (Stohl et al., 2000; Trickl et al., 2010).

Also, humid air from remote boundary layers sometimes causes rather intense short-term variations of the water vapor distribution. An example is shown in Fig. 11. The humidity profile shows a significant increase between 4 and 5 km a.s.l. within 2 h. Backward trajectory calculations from reanalysis data with the HYSPLIT vertical velocity model (see above) for this case suggest a sudden change in the source region from the North American upper troposphere (dry) to the northwest Pacific and rather low altitudes of about 2 km a.s.l. within 2 h (Fig. 12). In contrast, the air at an altitude of about 3.3 km constantly originates from the subtropical North Atlantic boundary layer (moderately humid, trajectories not shown here). The trajectory starting above the northwest Pacific Ocean exhibits a fast ascent to the upper tropo-

sphere within 2 days. This behavior is attributed to a warm conveyor belt using the criteria published by Eckhardt et al. (2004). Satellite images show that the ascending part of the blue trajectory is near the warm front of a cyclone that is located about 2000 km south of the peninsula of Kamchatka (northwest Pacific Ocean). Warm conveyor belts are known to be the most important extra-tropical transport mechanism of water vapor to the free and upper troposphere, although the water vapor flux moves like a jet from a rather restricted area (Browning and Roberts, 1994; Browning et al., 1997; Eckhardt et al., 2004; Ziv et al., 2009). It is remarkable that these filamentary structures are partially preserved, while traveling around half of the hemisphere. A wind speed of 16 m s^{-1} at an altitude of 4.5 km (Munich radiosonde, 12:00 UTC) transforms a time shift of 2 h into a horizontal shift of about 115 km. The water vapor density at this altitude changes by more than a factor of 5 within 2 h in this case.

5.2.2 General discussion

It is reasonable to assume that much of the variability in the free troposphere is caused by the rich layer structure advected along or in the vicinity of the North Atlantic storm track or from the Mediterranean basin and northern Africa. From our lidar measurements of ozone, water vapor, and aerosol, we know that the persistence of specific free-tropospheric layers above the Zugspitze can range from less than 1 h to more than 1 day (Eisele et al., 1999; Stohl and Trickl, 1999; Trickl et al., 2003, 2010, 2011). Along the jet stream, many different ascending and descending air streams merge or separate (e.g., Appenzeller et al., 1996; Stohl, 2001; Cooper et al., 2001, 2002, 2004a, b; Flentje et al., 2005). The advection of filamentary and heterogeneous layer structures affects the entire free troposphere and dominates the variability of water vapor in the upper troposphere above 5 km. The most important source regions contributing to observations above the Zugspitze are the stratosphere (very dry air), North America, the (sub)tropical Atlantic (very humid), and also Asia. Sometimes, dry and ozone-rich air flows along the northward spiraling subtropical jet streams (Trickl et al., 2011). The layers frequently possess a meridional component, leading to a transverse passage of adjacent layers across the observational site. This implies a rapid change in concentrations.

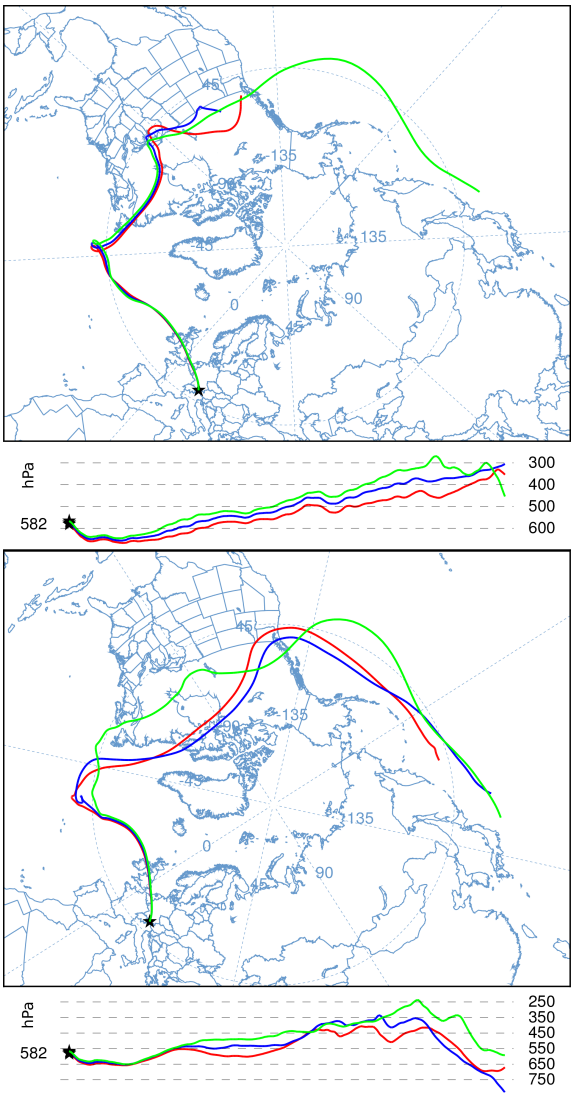

Figure 12. Backward trajectories from the NOAA HYSPLIT model (see text) ending above the Zugspitze at 4600, 4700 and 4800 m a.s.l. at 06:00 UTC (upper plot) and 08:00 UTC (lower plot), 29 July 2009 were calculated from reanalysis data with a vertical velocity model and a duration of 315 h. The vertical sections are referred to the air pressure along the pathways. The remarkable coherence of the three pathways during a longer time indicates a rather good reliability.

6 Summary and conclusions

The result of our studies is a quantitative description of the short-term variability of water vapor in the free troposphere above the Zugspitze, which is a location representative of central Europe. From measurement data recorded with two high-precision optical water vapor sounders arranged in a unique pointing geometry, we derived information about the spatiotemporal variability of integrated water vapor (IWV) on the scale of kilometers and of minutes.

Within a time interval of 20 min, a variability of about 0.35 mm was determined in the summer season under the condition of good volume matching ($\Delta x < 2$ km). The spatial variability became significant for horizontal distances above 2 km, but only in the warm season. The variability of IWV observed in the winter season was generally lower and did not increase with a horizontal mismatch of the probed volume ($\Delta x < 12$ km). Its relative value, however, was larger

than in the summer season. The seasonality of the IWV short-term variability and the geometrical restrictions of the measurements underline that local convection is the main source of variability during the warm season, while the variability in the winter season is driven by dynamics on a larger scale. The temporal variability of IWV was determined to be 0.05 mm on the scale of minutes (5 min) with a uniform increase to 0.5 mm on a timescale of 1 day.

The free-tropospheric profile variability of water vapor on the timescale of hours (e.g., 1–5 h) shows a broad minimum around 4.5 km a.s.l. and much larger values for higher altitudes with a constant increase up to the tropopause region. Longer time intervals generally yield larger variations at all altitudes and additionally show a more significant maximum at the lower edge of the measurement range (3 km). These findings are explained by the vertical wind profile and the heterogeneity of air masses within the upper air flow advected with a high velocity and, additionally, by the impact of local convection below 4.5 km. The covariance matrix of the profile variability yields information about the coherence of neighboring layers and shows that the air flow below 6 km is rather incoherent, while the upper air stream above 8 km is much more coherent.

We presented four case studies in which the profile variability of water vapor on the timescale of hours was attributed to specific mechanisms: local and vertically limited convection under stable conditions, high-reaching convection under unstable conditions, downwelling of a stratospheric intrusion, and long-range transport from very different source regions.

The source of the variability can be either local convection or long-range transport of inhomogeneous air masses. When reviewing all profiles of our study, we found that it is not always possible to distinguish clearly between both mechanisms of short-term variability. In particular, for altitudes below 4.5 km, which are potentially affected by local convection even under stable atmospheric conditions, we must assume a mixture of both local contributions and the advection of inhomogeneous layer structures from different remote source regions. From cases where a clear assignment was possible, we conclude that the long-range advection of very inhomogeneous layer structures can cause relative short-term variations of the water vapor concentration at a certain altitude, which are larger by 1 order of magnitude than variations in cases dominated by the impact of local convection. Due to the high altitude of the measurement site, our analysis is mostly restricted to the free troposphere. The upper edge of the Alpine boundary layer reaches our measurement range usually only during afternoons in the summer season. The consequence of measuring above a complex alpine terrain (steep mountain slopes) is that we observe the influence of local convection in our measurement range (above 3 km a.s.l.) quite frequently. The impact of local convection undercuts the possible impact of long-range transport by roughly 1 order of magnitude. This suggests, at least for the summer season, that the variability inside the boundary layer is probably reduced to values that we observe with dominating local convection reaching our measurement range. This assumption, of course, implies that the fast advection of heterogeneous air layers does not impact the boundary layer. However, the reported IWV variability during the warm season with dominating local convection, in principle, supports the findings from a recent IWV variability assessment by Steinke et al. (2015), although the underlying IWV determination started at lower altitudes and above less complex terrain. This less complex terrain assumably justifies our observations of relative short-term variations of about a factor of 2 higher of IWV in summer.

In spite of the missing convection, the relative short-term variability of water vapor (IWV and profiles) in the free troposphere is higher during the winter season. This is explained by the results of Trickl et al. (2010), according to which stratospheric air intrusions above the Zugspitze exhibit a pronounced maximum during the winter season. Roughly three-fourths of them reach the Zugspitze summit (2962 m) and were detected directly by the in situ instrumentation.

Our results for the first time provide a quantitative description of the free-tropospheric spatiotemporal variability of water vapor on the scales of minutes and kilometers (horizontal) for IWV and the scales of hours and 500 m (vertical) for profiles. This information can be useful for the parameterization of humidity in atmospheric models as well as for estimating the influence of the atmospheric variability of water vapor on the significance of water vapor measurements performed with a given integration time. In a related sense, our results also provide the information necessary for evaluating intercomparison studies of imperfectly co-located or synchronized instruments. Our findings fit perfectly with the results of our previous intercomparison study (Vogelmann et al., 2011) that indicated a high variability of water vapor, as a result of which, very tight matching criteria are required down to the scales of 10 min and several hundred meters to reduce co-location effects to a negligible level.

Acknowledgements. We thank Hans-Peter Schmid (KIT/IMK-IFU) for his continuous interest in this work and M. Rettinger (KIT/IMK-IFU) for executing the FITR measurements at the Zugspitze. We also thank Michael Sprenger (ETH Zürich) for providing the forward trajectory calculations (for the analysis of stratosphere-to-troposphere transport). We also acknowledge the team of the Schneefernerhaus research station (UFS) for maintaining our lidar measurements and the Bavarian Ministry of Environment and Consumer Protection for funding our work within the ALOMAR cooperation.

The article processing charges for this open-access publication have been covered by a Research Centre of the Helmholtz Association.

Edited by: M. Tesche

References

Adam, M., Demoz, B. B., Whiteman, D. N., Venable, D. D., Joseph, E., Gambacorta, A., Wei, J., Shephard, M. W., Miloshevich, L. M., Barnet, C. D., Herman, R. L., Fitzgibbon, J., and Connell, R.: Water Vapor Measurements by Howard University Raman Lidar during the WAVES 2006 Campaign, J. Atmos. Ocean. Tech., 27, 42–60, doi:10.1175/2009JTECHA1331.1, 2010.

Appenzeller, C., Davies, H. C., and Norton, W. A.: Fragmentation of stratospheric intrusions, J. Geophys. Res., 101, 1435–1456, doi:10.1029/95JD02674, 1996.

Birner, T., Dörnbrack, A., and Schumann, U.: How sharp is the tropopause at midlatitudes?, Geophys. Rev. Lett., 29, 1700, doi:10.1029/2002GL015142, 2002.

Bleisch, R., Kämpfer, N., and Haefele, A.: Retrieval of tropospheric water vapour by using spectra of a 22 GHz radiometer, Atmos. Meas. Tech., 4, 1891–1903, doi:10.5194/amt-4-1891-2011, 2011.

Browning, K. A. and Roberts, N. M.: Structure of a frontal cyclone, Q. J. Roy. Meteor. Soc., 120, 1535–1557, doi:10.1002/qj.49712052006, 1994.

Browning, K. A., Roberts, N. M., and Illingworth, A. J.: Mesoscale analysis of the activation of a cold front during cyclogenesis, Q. J. Roy. Meteor. Soc., 123, 2349–2375, doi:10.1002/qj.49712354410, 1997.

Carnuth, W. and Trickl, T.: Transport studies with the IFU three-wavelength aerosol lidar during the VOTALP Mesolcina experiment, Atmos. Environ., 34, 1425–1434, 2000.

Carnuth, W., Kempfer, U., and Trickl, T.: Highlights of the tropospheric lidar studies at IFU within the TOR project, Tellus, 54B, 163–185, 2002.

Cooper, O. R., Moody, J. L., Parrish, D. D., Trainer, M., Ryerson, T. B., Holloway, J. S., Hübler, G., Fehsenfeld, F. C., Oltmans, S. J., and Evans, M. J.: Trace gas signatures of the airstreams within North Atlantic cyclones: Case studies from the North Atlantic Regional Experiment (NARE 97) aircraft intensive, J. Geophys. Res., 106, 5437–5456, doi:10.1029/2000JD900574, 2001.

Cooper, O. R., Moody, J. L., Parrish, D. D., Trainer, M., Holloway, J. S., Hübler, G., Fehsenfeld, F. C., and Stohl, A.: Trace gas composition of midlatitude cyclones over the western North Atlantic Ocean: A seasonal comparison of O_3 and CO, J. Geophys. Res., 107, 4057, doi:10.1029/2001JD000902, 2002.

Cooper, O., Forster, C., Parrish, D., Dunlea, E., Hübler, G., Fehsenfeld, F., Holloway, J., Oltmans, S., Johnson, B., Wimmers, A., and Horowitz, L.: On the life cycle of a stratospheric intrusion and its dispersion into polluted warm conveyor belts, J. Geophys. Res., 109, D23S09, doi:10.1029/2003JD004006, 2004a.

Cooper, O. R., Forster, C., Parrish, D., Trainer, M., Dunlea, E., Ryerson, T., Hübler, G., Fehsenfeld, F., Nicks, D., Holloway, J., de Gouw, J., Warneke, C., Roberts, J. M., Flocke, F., and Moody, J.: A case study of transpacific warm conveyor belt transport: Influence of merging airstreams on trace gas import to North America, J. Geophys. Res., 109, D23S08, doi:10.1029/2003JD003624, 2004b.

Draxler, R. R. and Hess, G. D.: An Overview of the HYSPLIT_4 Modelling System for Trajectories, Dispersion, and Deposition, Australian Meteorological Magazine, 47, 295–308, 1998.

Eckhardt, S., Stohl, A., Wernli, H., James, P., Forster, C., and Spichtinger, N.: A 15-Year Climatology of Warm Conveyor Belts., J. Climate, 17, 218–237, doi:10.1175/1520-0442(2004)017<0218:AYCOWC>2.0.CO;2, 2004.

Eisele, H., Scheel, H. E., Sládkovič, R., and Trickl, T.: High-Resolution Lidar Measurements of Stratosphere-Troposphere Exchange, J. Atmos. Sci., 56, 319–330, 1999.

Fassò, A., Ignaccolo, R., Madonna, F., Demoz, B. B., and Franco-Villoria, M.: Statistical modelling of collocation uncertainty in atmospheric thermodynamic profiles, Atmos. Meas. Tech., 7, 1803–1816, doi:10.5194/amt-7-1803-2014, 2014.

Flentje, H., Dörnbrack, A., Ehret, G., Fix, A., Kiemle, C., Poberaj, G., and Wirth, M.: Water vapor heterogeneity related to tropopause folds over the North Atlantic revealed by airborne water vapor differential absorption lidar, J. Geophys. Res., 110, D03115, doi:10.1029/2004JD004957, 2005.

Harries, J. E.: Atmospheric radiation and atmospheric humidity, Q. J. R. Meteor. Soc., 123, 2173–2186, 1997.

Immler, F. J., Dykema, J., Gardiner, T., Whiteman, D. N., Thorne, P. W., and Vömel, H.: Reference Quality Upper-Air Measurements: guidance for developing GRUAN data products, Atmos. Meas. Tech., 3, 1217–1231, doi:10.5194/amt-3-1217-2010, 2010.

Kämpfer, N., Ed.: Monitoring Atmospheric Water Vapour - Ground-Based Remote Sensing and In-situ Methods, Springer, Berlin, Heidelberg, 2013.

Kiehl, J. T. and Trenberth, K. E.: Earth's Annual Global Mean Energy Budget, B. Am. Meteorol. Soc., 78, 197–208, 1997.

Kreipl, S.: Messung des Aerosoltransports am Alpennordrand mittels Laserradar (Lidar), Dissertation (in German), Universität Erlangen, 2006.

Leblanc, T., Walsh, T. D., McDermid, I. S., Toon, G. C., Blavier, J.-F., Haines, B., Read, W. G., Herman, B., Fetzer, E., Sander, S., Pongetti, T., Whiteman, D. N., McGee, T. G., Twigg, L., Sumnicht, G., Venable, D., Calhoun, M., Dirisu, A., Hurst, D., Jordan, A., Hall, E., Miloshevich, L., Vömel, H., Straub, C., Kampfer, N., Nedoluha, G. E., Gomez, R. M., Holub, K., Gutman, S., Braun, J., Vanhove, T., Stiller, G., and Hauchecorne, A.: Measurements of Humidity in the Atmosphere and Validation Experiments (MOHAVE)-2009: overview of campaign operations and results, Atmos. Meas. Tech., 4, 2579–2605, doi:10.5194/amt-4-2579-2011, 2011.

Müller, H. and Reiter, R.: Untersuchung der Gebirgsgrenzschicht über einem großen Alpental bei Berg-Talwindzirkulation, Meteorol. Rdsch., 39, 247–256 (in German), 1986.

Pougatchev, N. S., Connor, B. J., and Rinsland, C. P.: Infrared measurements of the ozone vertical distribution above Kitt Peak, J. Geophys. Res., 100, 16689–16697, doi:10.1029/95JD01296, 1995.

Reiter, R., Müller, H., Sladkovic, R., and Munzert, K.: Aerologische Untersuchungen der tagesperiodischen Gebirgswinde unter besonderer Berücksichtigung des Windfeldes im Talquerschnitt, Meteorol. Rdsch., 36, 225–242 (in German), 1983.

Riehl, H.: Jet Streams of the Atmosphere, Tech. Rep. 32, Department of Atmospheric Science Colorado State University Fort Collins, Colorado, 1962.

Seidel, D. J., Sun, B., Pettey, M., and Reale, A.: Global radiosonde balloon drift statistics, J. Geophys. Res., 116, D07102, doi:10.1029/2010JD014891, 2011.

Soden, B. J. and Lanzante, J. R.: An Assessment of Satellite and Radiosonde Climatologies of Upper-Tropospheric

Water Vapor., J. Clim., 9, 1235–1250, doi:10.1175/1520-0442(1996)009<1235:AAOSAR>2.0.CO;2, 1996.

Steinke, S., Eikenberg, S., Löhnert, U., Dick, G., Klocke, D., Di Girolamo, P., and Crewell, S.: Assessment of small-scale integrated water vapour variability during HOPE, Atmos. Chem. Phys., 15, 2675–2692, doi:10.5194/acp-15-2675-2015, 2015.

Stiller, G. P., Kiefer, M., Eckert, E., von Clarmann, T., Kellmann, S., García-Comas, M., Funke, B., Leblanc, T., Fetzer, E., Froidevaux, L., Gomez, M., Hall, E., Hurst, D., Jordan, A., Kämpfer, N., Lambert, A., McDermid, I. S., McGee, T., Miloshevich, L., Nedoluha, G., Read, W., Schneider, M., Schwartz, M., Straub, C., Toon, G., Twigg, L. W., Walker, K., and Whiteman, D. N.: Validation of MIPAS IMK/IAA temperature, water vapor, and ozone profiles with MOHAVE-2009 campaign measurements, Atmos. Meas. Tech., 5, 289–320, doi:10.5194/amt-5-289-2012, 2012.

Stohl, A.: A 1-year Lagrangian "climatology" of airstreams in the Northern Hemisphere troposphere and lowermost stratosphere, J. Geophys. Res., 106, 7263–7280, doi:10.1029/2000JD900570, 2001.

Stohl, A. and Trickl, T.: A textbook example of long-range transport: Simultaneous observation of ozone maxima of stratospheric and North American origin in the free troposphere over Europe, J. Geophys. Res., 104, 30445–30462, doi:10.1029/1999JD900803, 1999.

Stohl, A., Spichtinger-Rakowsky, N., Bonasoni, P., Feldmann, H., Memmesheimer, M., Scheel, H. E., Trickl, T., Hübener, S., Ringer, W., and Mandl, M.: The influence of stratospheric intrusions on alpine ozone concentrations, Atmos. Env., 34, 1323–1354, doi:10.1016/S1352-2310(99)00320-9, 2000.

Sun, B., Reale, A., Seidel, D. J., and Hunt, D. C.: Comparing radiosonde and COSMIC atmospheric profile data to quantify differences among radiosonde types and the effects of imperfect collocation on comparison statistics, J. Geophys. Res., 115, D23104, doi:10.1029/2010JD014457, 2010.

Sussmann, R. and Schäfer, K.: Infrared spectroscopy of tropospheric trace gases: combined analysis of horizontal and vertical column abundances, Appl. Opt., 36, 735–741, doi:10.1364/AO.36.000735, 1997.

Sussmann, R., Borsdorff, T., Rettinger, M., Camy-Peyret, C., Demoulin, P., Duchatelet, P., Mahieu, E., and Servais, C.: Technical Note: Harmonized retrieval of column-integrated atmospheric water vapor from the FTIR network – first examples for long-term records and station trends, Atmos. Chem. Phys., 9, 8987–8999, doi:10.5194/acp-9-8987-2009, 2009.

Tobin, D. C., Revercomb, H. E., Knuteson, R. O., Lesht, B. M., Strow, L. L., Hannon, S. E., Feltz, W. F., Moy, L. A., Fetzer, E. J., and Cress, T. S.: Atmospheric Radiation Measurement site atmospheric state best estimates for Atmospheric Infrared Sounder temperature and water vapor retrieval validation, J. Geophys. Res., 111, D09S14, doi:10.1029/2005JD006103, 2006.

Trenberth, K., Jones, P., Ambenje, P., Bojariu, R., Easterling, D., Tank, A., Parker, D., Rahimzadeh, F., Renwick, J., Rusticucci, M., Soden, B., and Zhai, P.: Observations: Surface and Atmospheric Climate Change. In Climate Change 2007: The Physical Science Basis. Contribution of Working Group I to the Fourth Assessment Report of the Intergovernmental Panel on Climate Change, chap. 3, 235–336, Cambridge, United Kingdom and New York, N.Y., USA, Cambridge University Press, 2007.

Trenberth, K. E.: Atmospheric Moisture Residence Times and Cycling: Implications for Rainfall Rates and Climate Change, Clim. Change, 39, 667–694, doi:10.1023/A:1005319109110, 1998.

Trickl, T., Cooper, O. R., Eisele, H., James, P., Mücke, R., and Stohl, A.: Intercontinental transport and its influence on the ozone concentrations over central Europe: Three case studies, J. Geophys. Res., 108, 8530, doi:10.1029/2002JD002735, 2003.

Trickl, T., Feldmann, H., Kanter, H.-J., Scheel, H.-E., Sprenger, M., Stohl, A., and Wernli, H.: Forecasted deep stratospheric intrusions over Central Europe: case studies and climatologies, Atmos. Chem. Phys., 10, 499–524, doi:10.5194/acp-10-499-2010, 2010.

Trickl, T., Eisele, H., Bärtsch-Ritter, N., Furger, M., Mücke, R., Sprenger, M., and Stohl, A.: High-ozone layers in the middle and upper troposphere above Central Europe: potential import from the stratosphere along the subtropical jet stream, Atmos. Chem. Phys, 11, 9343–9366, doi:10.5194/acp-11-9343-2011, 2011.

Trickl, T., Vogelmann, H., Giehl, H., Scheel, H.-E., Sprenger, M., and Stohl, A.: How stratospheric are deep stratospheric intrusions?, Atmos. Chem. Phys., 14, 9941–9961, doi:10.5194/acp-14-9941-2014, 2014.

Turner, D. D. and Mlawer, E. J.: The Radiative Heating in Underexplored Bands Campaigns, Bulletin of the American Meteorological Society, 91, 911–923, doi:10.1175/2010BAMS2904.1, 2010.

Vogelmann, H. and Trickl, T.: Wide Range Sounding of Free Tropospheric Water Vapor with a Differential Absorption Lidar (DIAL) at a High Altitude Station, Appl. Opt., 47, 2116–2132, doi:10.1364/AO.47.002116, 2008.

Vogelmann, H., Sussmann, R., Trickl, T., and Borsdorff, T.: Intercomparison of atmospheric water vapor soundings from the differential absorption lidar (DIAL) and the solar FTIR system on Mt. Zugspitze, Atmos. Meas. Tech., 4, 835–841, doi:10.5194/amt-4-835-2011, 2011.

Wagner, T., Beirle, S., Grzegorski, M., and Platt, U.: Global trends (1996-2003) of total column precipitable water observed by Global Ozone Monitoring Experiment (GOME) on ERS-2 and their relation to near-surface temperature, J. Geophys. Res., 111, D12102, doi:10.1029/2005JD006523, 2006.

Whiteman, D. N., Russo, F., Demoz, B., Miloshevich, L. M., Veselovskii, I., Hannon, S., Wang, Z., Vömel, H., Schmidlin, F., Lesht, B., Moore, P. J., Beebe, A. S., Gambacorta, A., and Barnet, C.: Analysis of Raman lidar and radiosonde measurements from the AWEX-G field campaign and its relation to Aqua validation, J. Geophys. Res., 111, D09S09, doi:10.1029/2005JD006429, 2006.

Wirth, M., Fix, A., Ehret, G., Reichardt, J., Begie, R., Engelbart, D., Vömel, H., Calpini, B., Romanens, G., Apituley, A., Wilson, K. M., Vogelmann, H., and Trickl, T.: Intercomparison of Airborne Water Vapour DIAL Measurements with Ground Based Remote Sensing and Radiosondes within the Framework of LUAMI 2008, in: Proceedings of the 8th International Symposium on Tropospheric Profiling, edited by: Apituley, A., Russchenberg, H., and Monna, W., Delft, the Netherlands, poster presentation, 2009.

Ziv, B., Saaroni, H., Romem, M., Heifetz, E., Harnik, N., and Baharad, A.: Analysis of conveyor belts in winter Mediterranean cyclones, Theor. Appl. Climatol., 99, 441–455, doi:10.1007/s00704-009-0150-9, 2009.